

Comparison of Donor-Acceptor π -Conjugated Dyes in Model Solar Cells: A Study of Interfacial Ultrafast Electron Migration

Gunter Hermann,* Felix Witte,* and Jean Christophe Tremblay*
(Dated: February 10, 2022)

Interfacial ultrafast electron migration processes are simulated in finite cluster models of dye-sensitized solar cells within a single active electron approach. Initially, three different donor-acceptor π -conjugated dyes supported on colloidal titania clusters are compared from the perspective of their optical and electronic properties. The potential performance of the model solar cell devices for charge migration processes is predicted from a static perspective. For this purpose, parameter-free expressions for state-resolved injection times and currents are established and evaluated for the three systems. A broadband laser excitation promoting the excited states in the visible region initiates the electron migration process. The evolution of the electronic wave packet is analyzed with a density-based toolset including the electronic yields partitioned for characteristic fragments of the model complexes and the time-dependent one-electron density for distinctive time steps in the dynamics. On the one hand, these reveal a microscopic picture for the mechanistic pathway of the charge migration and on the other hand, they validate the results from the time-independent analysis concerning the photovoltaic efficiency.

I. INTRODUCTION

Dye sensitized solar cells (DSSC), also known as Grätzel cells, are promising candidates to satisfy in the long-term the steadily growing global energy demand for an environmentally sustainable energy source.[1–8] This prospect is substantiated by their ability to capture and directly convert solar light into electrical current with high efficiency.[9–12] That in turn qualifies them as potential alternatives to conventional silicon-based photovoltaic devices. In general, these Grätzel type solar cells assemble transition-metal or organic dye molecules with a wide band gap semiconductor, such as titanium dioxide (TiO_2). This functionalization of semiconductor surfaces influences their electronic and optical properties and enables DSSCs the harvesting of sun light. The photonic energy conversion in DSSCs starts with the adsorption of incident light. This initiates the excitation of the dye from its ground state to an excited state. The latter is energetically located in the semiconductor conduction band. The photo-excited electron is then transferred to the semiconductor substrate on an ultrafast time scale typically ranging from femto- to picoseconds.[13, 14] Immediately, a charge separation occurs at the interface between the dye and the substrate. Ensuingly, the electron flows to one of the electrodes, and the oxidized dye is regenerated by the redox mediator, such as $[\text{Cu}(\text{dmp})_2]^{+1/+2}$ [15] or TEMPO[16], in the surrounding solution. In turn, this redox pair is restored at the counter electrode. The photoinduced electron-hole pair separation is the key step for the direct conversion of sunlight into electrical energy in DSSCs and thus influences its performance. The efficiency of this process strongly depends on the structural, optical, and elec-

tronic properties of the dye/semiconductor system, especially the proper alignment of their energy levels.[17–19] Consequently, the choice of the dye is crucial for a beneficial surface sensitization of the semiconductor.

Besides transition-metal dyes yielding the highest conversion efficiencies,[20, 21] the burgeoning group of metal-free organic chromophores have attracted particular interest. They stand out by their tunable optical properties, reduced environmental impact, low-cost, and rather simple synthetic routes.[22–25] In particular, donor-acceptor π -conjugated photosensitizers based on pyridinium are promising representatives.[26–28] They are based on an expanded π -conjugated moiety with a pyridinium core as electron acceptor, an amino group as electron donor, and a carboxylate group anchored to the semiconductor substrate. Its high photovoltaic performance relies on the broad and intense sunlight absorption of the π -conjugated system and the efficient charge separation in the dye due to the wide spatial separation of the electron releasing and electron withdrawing groups.[29, 30]

A myriad of theoretical[31–36] and experimental[37–40] studies has been conducted in the recent years with particular focus on the characterization of the spectroscopic and electronic properties of a multitude of different DSSCs and on the examination of the ultrafast charge injection.[41, 42] All of these follow the general aim of gaining information about the potential photovoltaic performance of the different chromophores supported on a TiO_2 substrate. In this context, the light absorption, the energetic alignment, and the electron injection times of DSSCs are pivotal properties which influence their photon-to-current conversion efficiency. From a theoretical point of view, these characteristics are chiefly extracted from static electronic structure calculations at the density functional theory (DFT) level, and from absorption spectra from linear-response time-dependent DFT (TDDFT).[43, 44] Within a single particle approach, we are aiming to ascertain these properties

* Institut für Chemie und Biochemie, Freie Universität Berlin, Takustraße 3, 14195 Berlin, Germany

using finite cluster models in a comparative study for three of these so-called push-pull dyes attached to a colloidal TiO_2 substrate. This approach has been proven to be reliable to describe such solar cell complexes.[45, 46] In this framework, we advocate calculating absorption spectra and projected density of states (pDOS) and elaborating parameter-free expressions for the state-resolved injection times and currents. In addition, we put special emphasis on time-resolved simulations of ultrafast interfacial charge migration processes in the model devices. These are described by time-dependent one-electron equations of motion and are initiated with a broadband laser excitation. In order to unveil the mechanistic features of the electron dynamics, we rely on a density-based diagnostic toolset which has demonstrated its suitability in previous studies of charge migration processes.[45, 47, 48] This toolset includes the projection of the electronic yield onto characteristic molecular fragments of the DSSCs and time-dependent electron densities. These highlight the correlation between the structural features of the dyes and the mechanistic pathway of the charge migration process.

The remainder of this paper is structured as follows: The composition of the model systems and the theoretical methodology to characterize and analyze the properties of the solar cell devices and to simulate the ultrafast charge migration process are outlined in Sec. II. The subsequent section presents the static characterization of the model complexes and the laser-driven electron dynamics revealing the system's photovoltaic performance. The most significant findings are summarized in the last section.

II. MODEL SYSTEMS AND THEORY

In this work, the light-induced interfacial electron migration processes in dye-semiconductor solar cell systems are simulated in real time and at an atomistic level of theory. The essential prerequisites to perform and analyze the dynamical simulation as well as the studied model solar cells are described below.

A. Construction of the Model Systems

The model systems for the dye-sensitized solar cells are constructed as finite cluster models, where a chromophore is attached to a colloidal TiO_2 nanocluster. Three different organic dyes are investigated concerning their performance and efficiency as photosensitizers. These three belong to the family of donor-acceptor π -conjugated dyes possessing a similar architecture. The common structural features of these push-pull dyes comprise an electron releasing group and an electron withdrawing group. In the present dyes, the latter is a conjugated π -system consisting of a pyridinium core expanded by three benzene rings. Two of the dyes (**B1** and **B2**)

exhibit a branched structure for the electron acceptor moiety, where the benzene rings are not directly bound to each other. In the third dye (**F1**), the rings and the pyridinium core are fused to a flat, rigid, and strongly conjugated π -system. The respective nomenclature, i.e., **B** for branched and **F** for fused, stems from Ciofini and coworkers, who have previously investigated these dyes from a purely static point of view.[30] Their findings have revealed advantageous electrochemical and optical properties of these dyes. As electron donor group, two different types of amino groups are investigated: a primary amino group ($-\text{NH}_2$) for **B1** and **F1** and a dimethyl amino group ($-\text{NMe}_2$) for **B2**. In the model solar cells, the dyes are anchored to the colloidal TiO_2 nanoparticle via a carboxylate group with a bidentate bridging attachment. This binding mode is typical for carboxylate groups resulting in a relatively strong chromophore-semiconductor coupling.[49, 50] The titania nanostructure is composed of 15 TiO_2 units and corresponds to a free-standing nanoparticle in solution. The starting point for its optimized geometry is a spherically shaped particle suspended in a polar solvent, ethanol. Its cluster size is chosen in accordance with the work of Sánchez-de Armas *et al.*[51], who demonstrated that this moderate sized nanocrystallite is sufficient to recover the electronic and optical properties of experimentally investigated dye-sensitized solar cells. The optimized geometry of all three model solar cell devices is depicted in Fig. 1.

B. Dynamical Simulation

In this work, the light-induced electron migration processes in dye-sensitized solar cells are described within a time-dependent single active electron approach. The real-time propagation of the electron dynamics is performed by solving the one-particle non-relativistic time-dependent Schrödinger equation[52]

$$i\hbar \frac{\partial}{\partial t} \Psi_{\text{el}}(\mathbf{r}, t) = \hat{H}(\mathbf{r}, t) \Psi_{\text{el}}(\mathbf{r}, t). \quad (1)$$

Here, $\Psi_{\text{el}}(\mathbf{r}, t)$ is the time-dependent one-particle electronic wavefunction, and $\hat{H}(\mathbf{r}, t)$ signifies the total time-dependent Hamiltonian. In general, the interfacial electron migration process in a dye-sensitized solar cell comprises three essential steps: Firstly, the photoexcitation of the chromophore, secondly, the migration of the photoelectron from the dye into the colloidal semiconductor substrate, and thirdly, the absorption of the electron at the edges of the titania cluster to simulate the contact with an infinite electrode. To capture all these steps, the total Hamiltonian is modeled as follows

$$\hat{H}(\mathbf{r}, t) = \hat{H}_0(\mathbf{r}) + \hat{H}_{\text{field}}(t) - \hat{W}_{\text{CAP}}, \quad (2)$$

where $\hat{H}_0(\mathbf{r})$ is the field-free time-independent electronic Hamiltonian, $\hat{H}_{\text{field}}(t)$ characterizes the interaction of the

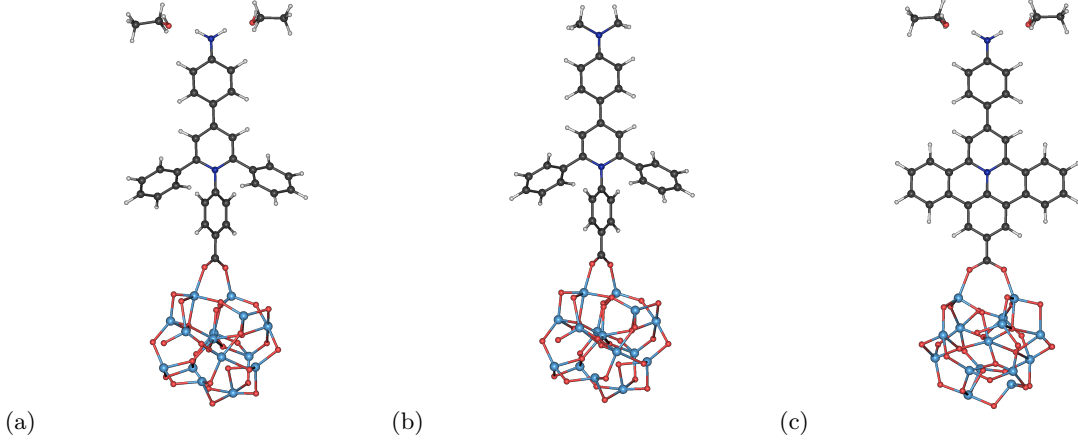


FIG. 1. Ball-and-stick models of the optimized molecular structures of the three different dyes, (a) **B1**, (b) **B2**, and (c) **F1**, attached to a colloidal TiO_2 nanocluster. The carbon, hydrogen, nitrogen, oxygen, and titanium atoms are represented as dark gray, light gray, blue, red, and cyan beads, respectively.

system with a time-dependent field, and \hat{W}_{CAP} is a complex absorbing potential.

In the present single active electron approach, the evolution of the electronic structure of the system out of equilibrium is obtained from the time-dependent electronic wave function which is defined as an expansion in a basis of stationary one-particle functions

$$\Psi_{\text{el}}(\mathbf{r}, t) = \sum_{\lambda=0} C_{\lambda}(t) \varphi_{\lambda}(\mathbf{r}). \quad (3)$$

Here, $C_{\lambda}(t)$ signifies the expansion coefficients of the electronic state λ , and $\varphi_{\lambda}(\mathbf{r})$ are the respective time-independent one-particle eigenfunctions. The latter satisfy the stationary one-particle electronic Schrödinger equation

$$\hat{H}_0(\mathbf{r}) \varphi_{\lambda}(\mathbf{r}) = E_{\lambda} \varphi_{\lambda}(\mathbf{r}). \quad (4)$$

A single occupied orbital describes the initial state, which can be promoted to several excited orbitals. This computational setup corresponds to a restricted active space configuration interaction singles scheme.[53] To obtain the time-evolution of the coefficients $C_{\lambda}(t)$, the equations of motion are integrated numerically using an adaptive step size Runge-Kutta algorithm, as implemented in our in-house program package ρ -TDCI. A detailed description can be found elsewhere.[54–56]

The eigenfunctions $\varphi_{\lambda}(\mathbf{r})$ are derived from first-principles electronic structure calculations at the DFT level and thus coincide with Kohn-Sham (KS) orbitals $\varphi_{\lambda}(\mathbf{r})$. In the MO-LCAO (Molecular Orbital-Linear Combination of Atomic Orbitals) ansatz, these KS orbitals are expanded as a linear combination of a finite set of atomic orbitals $\psi_i(\mathbf{r} - \mathbf{R}_A)$

$$\varphi_{\lambda}(\mathbf{r}) = \sum_A \sum_i^{N_{\text{AO}}} D_{\lambda i} \psi_i(\mathbf{r} - \mathbf{R}_A), \quad (5)$$

where $D_{\lambda i}$ is the i th MO coefficient for the MO λ , N_A denotes the number of atoms, and N_{AO} stands for the number of atomic orbitals. In this approach, the energies of the eigenstates (cf. Eq. 3) correspond to the KS orbital energies, and the Highest-Occupied MO (HOMO) is typically selected as the orbital containing the active electron. Since the HOMO is usually located on the dye, the photoexcitation in DSSCs is dominantly driven by intramolecular transitions between the HOMO and several virtual orbitals. Thus, an appropriate selection of virtual KS orbitals is required to properly simulate the excitation dynamics. In accordance to the usage of KS orbitals, the time-dependent single active electron ansatz is referred to as TDKS. The excitation dominated by a HOMO-LUMO character obtained from linear-response TDDFT is used to scale the fundamental gap of the KS orbitals.

In order to photoexcite the DSSC model system, the semiclassical dipole approximation is used for $\hat{H}_{\text{field}}(t)$

$$\hat{H}_{\text{field}}(t) = -\hat{\boldsymbol{\mu}} \cdot \mathbf{F}(t) \quad (6)$$

with $\hat{\boldsymbol{\mu}}$ as molecular dipole operator. A superposition of linearly polarized laser fields $\mathbf{F}(t)$ with a \sin^2 -shape

$$\mathbf{F}(t) = \sum_k \mathbf{f}_k(t) \cos(\omega_k t), \quad (7)$$

$$\mathbf{f}_k(t) = \begin{cases} \mathbf{f}_{k,0} \sin^2\left(\frac{\pi t}{t_{k,f}}\right) & \text{if } 0 < t < t_{k,f} \\ 0 & \text{else,} \end{cases}$$

is applied to promote several excited states from the initial state. In all simulations, the system is initially found in the ground state, which is represented here by the HOMO. In Eq. 7, the carrier frequency of the laser pulse k , its pulse length, and its amplitude are designated by ω_k , $t_{k,f}$, and $\mathbf{f}_{k,0}$, respectively. Here, the carrier frequencies correspond to the difference energy between the ground state and the target states.

Since the electron migration process is simulated in a finite Ti_2O nanocrystallite, a complex absorbing potential $\hat{W}_{\text{CAP}} = \sum_{\lambda} \gamma_{\lambda} |\varphi_{\lambda}\rangle \langle \varphi_{\lambda}|$ (cf. Eq. 2) is employed to suppresses artificial recurrences in the electron dynamics and reflections at the boundary of the model DSSC. To this end, we partition the time-independent Hamiltonian as

$$\begin{aligned} \hat{H}_0 &= (\hat{P} + \hat{Q}) \hat{H}_0 (\hat{P} + \hat{Q}) \\ &= \hat{P} \hat{H}_0 \hat{P} + (\hat{P} \hat{H}_0 \hat{Q} + \hat{Q} \hat{H}_0 \hat{P}) + \hat{Q} \hat{H}_0 \hat{Q}, \end{aligned} \quad (8)$$

where \hat{P} is the Mulliken projector on the interfacial oxygen atoms, and $\hat{Q} = 1 - \hat{P}$ is its complement. We define the absorbing potential as the hopping term from the dye-cluster system to the interface, where the electron is absorbed at the rate γ_{λ} . The associated intrinsic lifetime $\tau_{\lambda} = \gamma_{\lambda}^{-1}$ of state λ can be evaluated using first order time-dependent perturbation theory

$$\begin{aligned} \gamma_{\lambda} &= \frac{\pi}{\hbar} \left| \left\langle \varphi_{\lambda} \left| \hat{W}_{\text{CAP}} \right| \varphi_{\lambda} \right\rangle \right|^2 \delta(E_{\lambda} - E_{\lambda}) \\ &= \frac{\pi}{\hbar} \left| \left\langle \varphi_{\lambda} \left| \hat{P} \hat{H}_0 \hat{Q} + \hat{Q} \hat{H}_0 \hat{P} \right| \varphi_{\lambda} \right\rangle \right|^2 \delta(E_{\lambda} - E_{\lambda}) \\ &= \frac{\pi}{\hbar} \left| \sum_{\kappa \kappa'} \left\langle \varphi_{\lambda} \left| \hat{P} \right| \varphi_{\kappa} \right\rangle \left\langle \varphi_{\kappa} \left| \hat{H}_0 \right| \varphi_{\kappa'} \right\rangle \left\langle \varphi_{\kappa'} \left| \hat{Q} \right| \varphi_{\lambda} \right\rangle \right|^2 \\ &\quad + \text{c.c.} \delta(E_{\lambda} - E_{\lambda}) \\ &= \frac{\pi}{\hbar} \left| \sum_{\kappa} \left\langle \varphi_{\lambda} \left| \hat{P} \right| \varphi_{\kappa} \right\rangle E_{\kappa} \left\langle \varphi_{\kappa} \left| \hat{Q} \right| \varphi_{\lambda} \right\rangle \right|^2 \\ &\quad + \text{c.c.} \delta(E_{\lambda} - E_{\lambda}). \end{aligned} \quad (9)$$

Evaluation of the matrix element $\left\langle \varphi_{\lambda} \left| \hat{P} \right| \varphi_{\kappa} \right\rangle$ from the interfacial projector formalism[45, 57] is performed as

$$\left\langle \varphi_{\lambda} \left| \hat{P} \right| \varphi_{\kappa} \right\rangle = \sum_{A \in \text{O}} \sum_i^{N_{\text{AO}}} \sum_{j_A}^{N_{\text{AO}}} C_{\lambda j_A} C_{\kappa i} S_{j_A i}, \quad (10)$$

where $S_{j_A i} = \langle \psi_{j_A} | \psi_i \rangle$ is an element of the atomic orbital overlap matrix. The adsorption projector \hat{P} exclusively acts on the oxygen atoms at the bottom of the titania cluster of the model DSSC.

C. Static and Dynamical Analysis

In the scope of the present work, two main goals are pursued: first, the characterization of the static electronic and optical properties for our DSSC model systems, and second, the analysis and visualization of the dynamical mechanism of the photo-induced electron migration processes. For the first, the atom-projected density of states (pDOS) and the absorption spectra of the

model DSSCs are calculated from the KS orbitals to verify the proper energetic alignment between the dye and the TiO_2 cluster and to validate their spectroscopic properties. For this purpose, the excitation energies $\Delta E_{0\lambda}$ and the oscillator strength $f_{0\lambda}$ between the HOMO and a set of target virtual orbitals are necessary. The latter is defined as

$$f_{0\lambda} = \frac{2}{3} \frac{m_e}{e^2 \hbar^2} \Delta E_{0\lambda} \sum_{q=x,y,z} |\mu_{0\lambda,q}|^2 \quad (11)$$

with $\mu_{0\lambda,q}$ as the q th component of the dipole moment. In our laser-induced electron dynamics, the oscillation strength can be understood as the probability of an electronic transition, induced by the interaction with an absorbed photon, and the injection time as the time for the injection of the excited electron into the semiconductor of the DSSC. In addition, the current $I_{0\lambda}$ for this electronic state-to-state transition can be formulated from the oscillator strength $f_{0\lambda}$ and the absorption rate γ_{λ}

$$I_{0\lambda} = e f_{0\lambda} \gamma_{\lambda}. \quad (12)$$

Together, the injection time and the current, facilitates to assess the potential performance and efficiency of the electron injection process from a time-independent perspective.

The analysis of the real-time propagation of the electron migration processes is accomplished by means of a recently presented toolset.[45, 47] As an essential component, this comprises the time-dependent electron density

$$\rho(\mathbf{r}, t) = \Psi_{\text{el}}(\mathbf{r}, t) \Psi_{\text{el}}^{\dagger}(\mathbf{r}, t). \quad (13)$$

For a space-resolved analysis of the time-dependent electron density, the Voronoi partitioning scheme is employed.[58] This method assigns certain atoms or fragments to a set of points in space which are closest to them. Integrating the electron density over these Voronoi cells reveals the number of electrons in the respective spatial region

$$n_V(t) = \int_{\text{Voronoi cell of } V} d\mathbf{r} \rho(\mathbf{r}, t). \quad (14)$$

Based on the electron density and the Voronoi scheme, one can define a supplementary quantity to study the electron dynamics, i.e., the electronic yield

$$Y_V(t) = \int_0^t dt' \int_{\text{Voronoi cell of } V} d\mathbf{r} \frac{\partial \rho(\mathbf{r}, t')}{\partial t'} = n_V(t) - n_V(0). \quad (15)$$

This quantity determines the number of electrons that flow through a certain Voronoi cell within a time interval.[59]

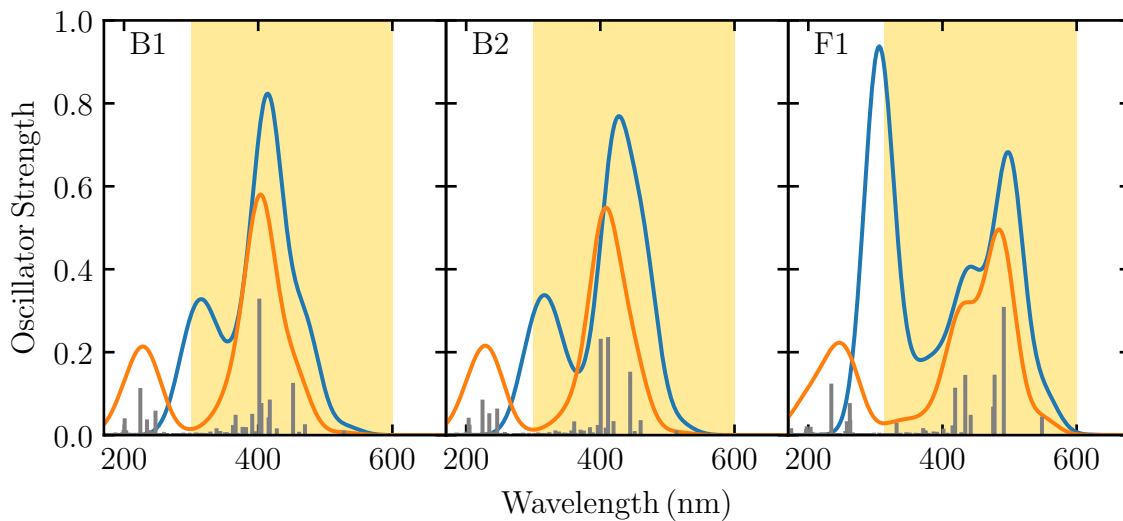


FIG. 2. Simulated optical spectra for the three extended pyridinium dyes, **B1**, **B2**, and **F1**, attached to a colloidal TiO_2 -cluster. Absorption spectra (orange) obtained from the broadened molecular orbital transition energies ($hc/\Delta E_{0\lambda}$) are shown along with the broadened spectra from the results of linear-response TDDFT calculations (blue). Both are based on a single-point calculation at the PBE0 level using a def2-SVP basis set. The molecular orbital transition energies corresponds to the difference energies between the HOMO and the virtual orbitals $\Delta E_{0\lambda}$. Gaussian functions with a width of $\sigma = 30$ nm are used to construct the spectra. Vertical gray lines represent the oscillator strengths of the specific transitions of the orange spectra. The oscillator strengths are calculated according to Eq. 11. The yellow region marks the first absorption band in each spectra. These excited states are stimulated in the electron dynamics.

III. RESULTS AND DISCUSSION

A. Computational Details

Based on the structural construction of the model DSSCs explained in Sec. II A, structure optimizations for the three dyes, **B1**, **B2**, and **F1**, attached to the colloidal $(\text{TiO}_2)_{15}$ nanocrystallite are carried out at the DFT level with the PBE0 functional[60] and the def2-SVP basis set[61, 62]. In addition, Grimme's dispersion correction D3(BJ) is employed to include the influence of dispersion effects.[63, 64] During the optimization process, the neutral dye-semiconductor complexes were allowed to freely relax. The continuum solvation model implemented in the COSMO-RS package[65–68] is used to mimic the suspension of the colloidal nanoparticles in an electrolyte, i.e., simulating the effects of ethanol as a solvent on the model DSSCs. In accordance to the work of Ciofini *et al.*, two explicit ethanol are coadsorbed to the primary amino group ($-\text{NH}_2$) in **B1** and **F1** to yield better optical properties. These are obtained from TDDFT[69] calculations in linear response to produce electronic absorption spectra for the DSSC complexes. As can be seen from previous work on electron charge migration in DSSCs, the electronic and spectroscopic properties could be accurately predicted with the particular selection of TDDFT/PBE0.[70, 71] All quantum chemical calculations are performed with TURBOMOLE[72]. For the dynamical simulation of the laser-induced charge migration, an in-house implementation of the ρ -TDCI

method[55, 56] is employed with 35 eigenstates in the dynamical basis. The ensuing static and dynamical analysis of the charge migration are executed with the Python toolbox ORBKIT[73] and the data visualization with the programs Amira[74] and matplotlib[75].

B. Static Properties of the Model Systems

The optimized structures of the three dye- TiO_2 model systems containing the three different chromophores, **B1**, **B2**, and **F1**, are depicted in Fig. 1. It can be seen in all three complexes that the benzene ring nearest to the titania cluster lies in plane with the two anchoring titanium atoms. In addition, the remaining part of the branched dyes, **B1** and **B2**, is twisted with respect to this aromatic ring. The respective dihedral angle between this benzene ring and the pyridinium core is 65.3° for **B1** and 66.1° for **B2**. The reason for this torsion is the reduction of steric hindrance between the benzene ring nearest to the TiO_2 -cluster and the two other freely rotatable benzene rings bound to the pyridinium core. This induces a weaker conjugation of these chromophores in comparison to the fused dye, **F1**. The pericondensation of the latter dye extends its π -conjugated system. These structural features influence the hybridization between the dye and the TiO_2 nanocluster, and thus the electronic coupling and energetic alignment between both. These are key factors which can crucially affect the charge migration process. Ensuingly, the optical spectra for the three DSSCs model devices are obtained from the linear-

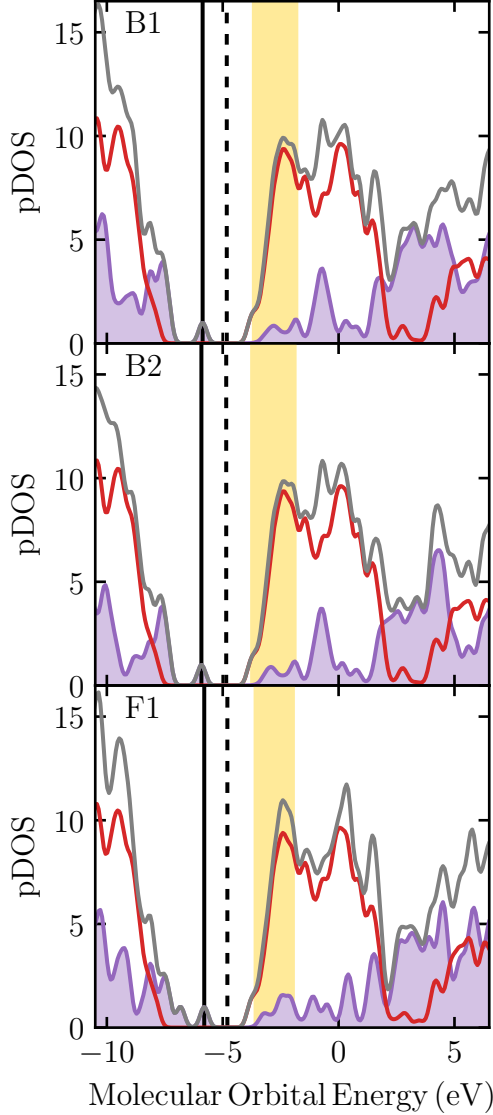


FIG. 3. Projected density of states (pDOS) for the three photosensitizer, **B1**, **B2**, and **F1**, coupled to a titania nanocluster. The states correspond to the one-electron molecular orbitals. The DOS is projected on the dye (purple), on the TiO_2 -cluster (red), and on the entire solar cell model system (gray). The solid black line signifies the HOMO and the dashed black line marks the Fermi energy (middle of HOMO-LUMO gap). All excited states which are photoexcited from the HOMO in the electron dynamics are located in the yellow region.

response TDDFT calculations using their PBE0 equilibrium geometries. For comparison purposes, the absorption spectra are computed on the basis of the MO energy differences between the HOMO and a set of virtual KS orbitals and the respective oscillator strengths, as defined in Eq. 11. Here, the HOMO-LUMO gap is adjusted to the optical gap obtained from the TDDFT results. A comparison between both methods, TDDFT (blue) and

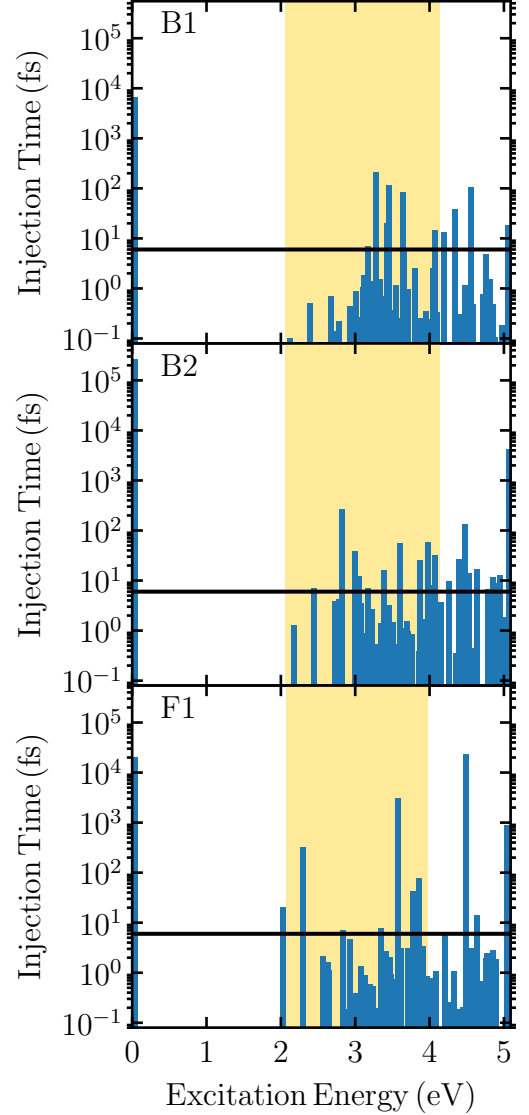


FIG. 4. Injection time τ_λ of the solar cell model systems with **B1**, **B2**, and **F1**, as a function of the excitation energy $\Delta E_{0\lambda}$. The yellow area signifies the region of light excitation in the dynamical propagation. The black horizontal line at 6 fs signifies a typical experimental injection time for similar solar cell devices.

KS (orange), is illustrated in Fig. 2. The TDDFT spectra show two broad bands for all three complexes, one in the visual region between 300 nm and 600 nm, and one in the UV-region. This shape can be likewise captured with the KS approach. From the experimental spectra of the single chromophores (cf. Ref. [29]), a similar shape of the absorption spectra can be recognized, where likewise a broad band exists in the visual region. As expected, this band is red-shifted due to the anchoring of the dye to the titania cluster. In the Supplementary Information, the comparison between both methods with reference to the experimental data can be found for the single

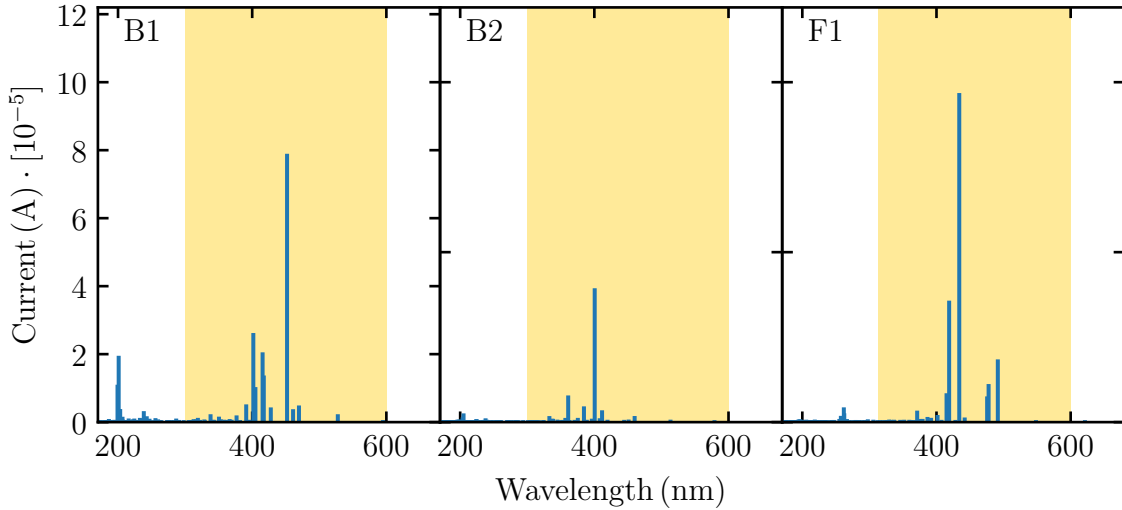


FIG. 5. Current $I_{0\lambda}$ (cf. Eq. 12) as a function of the wavelength ($hc/\Delta E_{0\lambda}$) for the three studied solar cells. The yellow area marks the first absorption band of each model system (cf. Fig. 2) which are excited in the dynamical simulation.

dyes. At first glance, the shape of the absorption spectra for the three complexes (cf. Fig. 2) is very similar, while the maxima of the first band is slightly red-shifted from **B1** to **F1**. This is a consequence of the different conjugation of the chromophores. As can be observed, the agreement between both methodologies for the first band is satisfactory, revealing a minor blue-shift. This is due to the fact that the dominant contributions for all excited states of the first band in the TDDFT reference are excitations from the HOMO to low-lying virtual orbitals. A density plot of the HOMO can be seen in Fig. 9 ($t = 0$ fs) which shows that it is mainly localized on the donor group of each dye. Consequently, a charge migration from this donor group to the acceptor group and finally into the TiO_2 cluster is expected during photoexcitation. The second band is rather poorly reproduced by the KS methodology, since transitions from other occupied orbitals except the HOMO are dominant in this region. Since excitation of the first band is advocated as photosensitizer in the visible frequency range, this would not affect the subsequent dynamical simulation. All states contributing to this band are marked as a yellow shaded area in all figures of the static analysis. To reveal details about the energetic alignment between the dye and the TiO_2 nanocluster, the pDOS are presented in Fig. 3 for the dye (purple) and the titania cluster (red), together with the pDOS of the complete model device (gray). In an indirect injection cell, the electron photoexcitation starts from the ground state localized on the chromophore, which lies energetically in the band gap of the substrate. The electron is then promoted to an excited state which is hybridized with the conduction band of the semiconductor. As can be seen from Fig. 3, this energetic alignment is reproduced by the single particle eigenstates of all three model DSSCs. That is, the HOMO marked with a black solid line is fully localized

on the chromophore and lies between states with dominant contributions from TiO_2 . The excited states with optical activity in the visible range are mainly located on the substrate, as indicated with the yellow filling. It is obvious that these states have a slightly higher contribution from the dye in the **F1**- TiO_2 -complex in comparison to the other two systems, which implies a higher degree of hybridization between the dye-localized HOMO and the excited states in the visual region. As a partial conclusion, one can state that our model devices correctly mimic the essential electronic and spectroscopic properties of a realistic DSSC, which makes them suitable for the time-dependent simulation of the electron transfer processes.

In the last step of the time-independent analysis, the possibly achievable photovoltaic performance of the three systems is deduced from a static view. For this purpose, the state-resolved injection times τ_λ and the currents $I_{0\lambda}$ for the transition between the HOMO and each one-electron excited state are determined. The former are depicted in Fig. 4, with a reference line corresponding to a typical experimental injection time of 6 fs (black horizontal line).^[14] It can be observed that only seven, twelve, and six of the excited states in **B1**, **B2**, and **F1** possess an injection time longer than the experimental guideline. The injection time of all other states in the respective region are in the regime of a few femtoseconds. Under the assumption that all designated target states can be equally excited from the ground state, the advocated charge migration process would proceed fastest for the **F1** dye.

To account for the excitation probability between the HOMO and the virtual orbitals, the associated currents $I_{0\lambda}$ are calculated from Eq. 12. Results for the three systems are reported in Fig. 5. For the targeted charge transfer states (yellow region), the total current obtained

by summing all state currents amounts to $1.71 \cdot 10^{-4}$ A, $5.95 \cdot 10^{-5}$ A, and $1.83 \cdot 10^{-4}$ A for **B1**, **B2**, and **F1**, respectively. It is apparent that the number of charge transfer states dominantly contributing to this overall current increases from **B2** to **B1** and **F1**. In the charge migration process, these states will be prevalently used by the photoexcited electron as channels for the injection from the dye into the TiO_2 substrate. It is interesting to note that one channel at ~ 450 nm is much more efficient in chromophore **F1**. This implies that **F1** is expected to lead to a faster, stronger electron injection upon photoexcitation. These tendencies match with the findings of Ciofini and co-workers.

C. Charge Migration Dynamics

The following section examines the differences in the electron transfer dynamics for the model solar cells with the three push-pull dyes, **B1**, **B2**, and **F1**. In this type of DSSCs, the charge migration is initiated by the photoexcitation of the dye, where the electron is transferred from the donor group of the dye (amino group) to its acceptor group (extended pyridinium core) and subsequently into the semiconductor substrate. The TiO_2 nanocrystallite is in contact with an electrode, which finally absorbs the electron. To simulate this process, all excited states (virtual orbitals) energetically lying in the visible region and building the first absorption band (indicated with a yellow filling in Fig. 2) are excited from the ground state (HOMO) with a superposition of \sin^2 -shaped pulses. Each single pulse is tuned to the carrier frequency for the respective state-to-state transition. As for the absorption spectra, the HOMO-LUMO gap is adjusted to the TDDFT optical energy gap. The pulse amplitude and duration (19 fs) are tailored to a typical laser pulse used in experimental studies of transient absorption measurements in similar DSSCs.[14, 76] The charge migration process is terminated by the absorption of the electron at the bottom of the titania nanocluster, as discussed in the previous section. This is accomplished by the absorption potential defined in Eq. 9 and 10 which concurrently inhibits unphysical reflections at the TiO_2 cluster edges. The propagation of the state populations in real time and the respective laser fields for the three systems in comparison are depicted in Fig. 6. At first glance, the results for the three solar cells reveal a similar course for the photoinduced charge migration. The ground state is depopulated in the first ~ 11 fs of the propagation during the laser pulse. The ground state population is transferred to a subset of excited states and subsequently absorbed by the potential at the bottom of the titania cluster. Despite targeting different sets of excited states for the three dyes, the laser fields for the broadband excitation have a similar frequency. However, the shape differs slightly between the two branched dyes, **B1** and **B2**, and the pericondensed dye, **F1**. The time-evolution of the state population for the three sys-

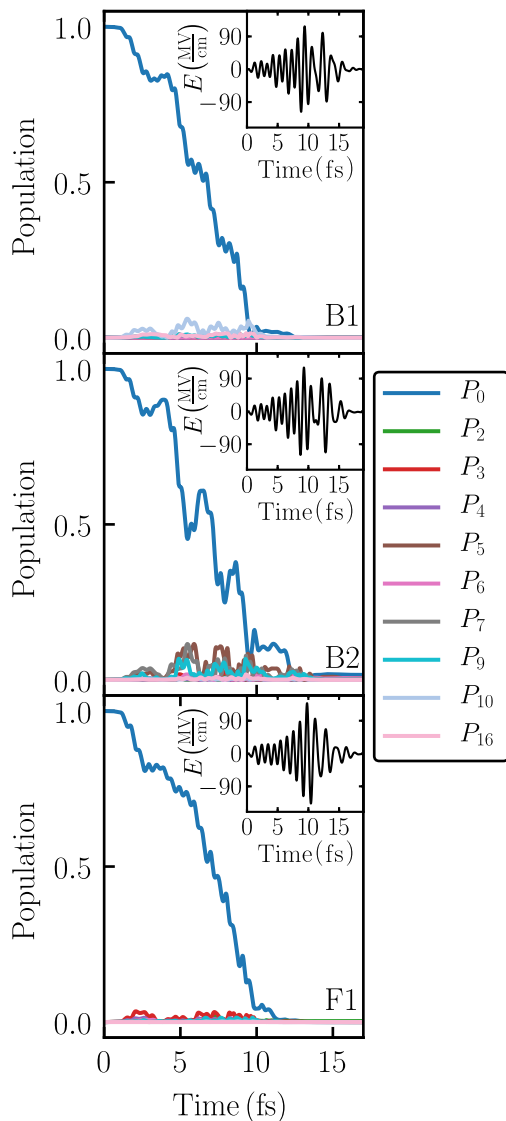


FIG. 6. Population propagation of the light-induced electron dynamics for the three different dyes, **B1**, **B2**, and **F1**, supported on a TiO_2 -cluster. A broadband excitation promotes the electron dynamics. All target states are located in the first absorption band of each model solar cell (cf. Fig. 2). The laser field is constructed from a superposition of state-to-state π -pulses with a duration of 19 fs. 35 states are incorporated in the electron dynamics.

tems exhibits distinct characteristics. On the one hand, the population oscillates differently between the ground state and a subset of excited states for the three systems. On the other hand, the number of significantly populated excited states increases from **F1** to **B2**. Both have an effect on the overall electron injection time. The differences can be explained as follows: The **B2** dye possesses longer-lived excited states. Accordingly, the coherent dynamics between these states and the ground state is maintained for a longer time period leading to a higher population

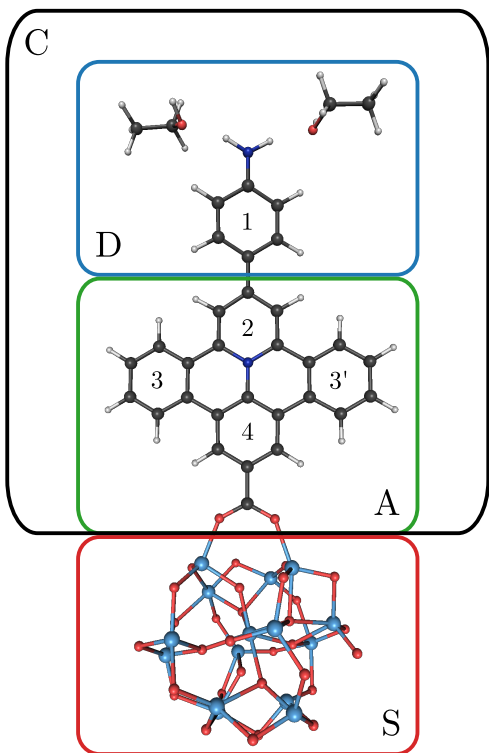


FIG. 7. Allocation of the Voronoi polyhedrons for the analysis of the electronic yield $Y_V(t)$. The boxes determine these particular Voronoi fragments in the respective model complexes. The chromophore (C), its electron donor group (D), its electron acceptor group (A), and the TiO_2 -substrate (S) are colored black, blue, green, and red, respectively. Dark gray, light gray, blue, red, and cyan beads represent the carbon, hydrogen, nitrogen, oxygen, and titanium atoms, respectively.

oscillation. In contrast, the excited states in **F1** are very short-lived, and the electron is rapidly injected into the TiO_2 -nanocrystallite. Hence, the excited states are only marginally populated, which results in a lower population oscillation with the ground state. Consequently, the injection process proceeds fastest for **F1**.

In order to refine the dynamical analysis, the electronic yields $Y_V(t)$ are calculated from Eq. 15 to reveal the mechanistic details of the electron dynamics. In relation to the common structural features of the model devices, the yield $Y_V(t)$ is divided into certain Voronoi polyhedrons comprising the dye (black, C), its electron donor moiety (blue, D), its electron acceptor group (green, A), and the semiconductor substrate (red, S). This partitioning scheme is represented in Fig. 7. The respective one-electron yields during the laser pulse are displayed in Fig. 8.

Once again, the three solar cell complexes show several similarities: First, the electron density synchronously fluctuates between the electron donating and withdrawing moieties and is continually injected into the titania nanocluster during this oscillation. Second, the yield curves for the complete dye and the substrate are rela-

tively smooth in contrast to the oscillatory pattern of the electron donor and acceptor groups. Third, the electron density that is injected into the TiO_2 -cluster is immediately absorbed, as can be seen from the almost constant red line. Here again, dye **B2** exhibits the most structure because the states are longer-lived and retain a coherent nature over a longer period of time. In accordance with the population evolutions, the oscillation of the electronic yields of the donor and acceptor groups has the largest magnitudes for the branched dyes. This indicates that the photoexcited electron in the **F1** dye is transferred from the amino group into the semiconductor in a more direct manner. This can be ascribed to the structural and electronic differences of the dyes. Considering our static and dynamic analysis, the strength of the charge transfer process is very sensitive towards the hybridization between the dye and the TiO_2 nanocrystallite, which is strongest for the **F1** dye (cf. Fig. 3). Besides, the slightly stronger electron donating property of the dimethyl amino group ($-\text{NMe}_2$) in comparison to the primary amino group ($-\text{NH}_2$) appears to decrease the charge transfer efficiency. This observation is in line with the studies of Ooyama and co-workers, who have investigated the influence of different substituents in a photosensitizer on the photovoltaic efficiency of DSSCs.[77]

The analysis of the structural properties influencing the charge migration is complemented by comparing time-dependent electron densities for chromophore **B1** with a branched framework with the pericondensed dye **F1**. Isosurface plots at characteristic time steps are depicted in Fig. 9. The time points are chosen such that the electron density has a maximal time-dependent yield at the electron donor group or at the electron acceptor group in order to display the fluctuation between both moieties. Gray vertical lines mark these points in the respective subplots in Fig. 8. Additionally, the initial time step ($t = 0$) is considered. For sake of clarity, the aromatic rings of the dyes are assigned in Fig. 7. The mechanism of the overall electron injection process can be summarized into two steps: First, electron density enrichment of the acceptor group (see second and fourth time step in Fig. 9) and second, the back transfer of electron density from the acceptor group to the donor group and the simultaneous electron injection into the TiO_2 -cluster (see third time step in Fig. 9). This oscillatory pattern is repeated until all electron density is absorbed at the bottom of the semiconductor. In greater detail, it can be observed that the electron moves directly from the amino group through the benzene rings 2 and 4 to the substrate. This electron loss appears to be monotonic. The electron density which is transferred to the rings 3 and 3', is partially transferred back to the electron releasing group (ring 1). This effect seems to be increased for the branched dye **B1**, since there is no direct injection channel. In addition, the torsion between ring 4 and the pyridinium core decreases the hybridization between both fragments, which appears to reduce the injection rate. Concluding these observations, a large conjugation

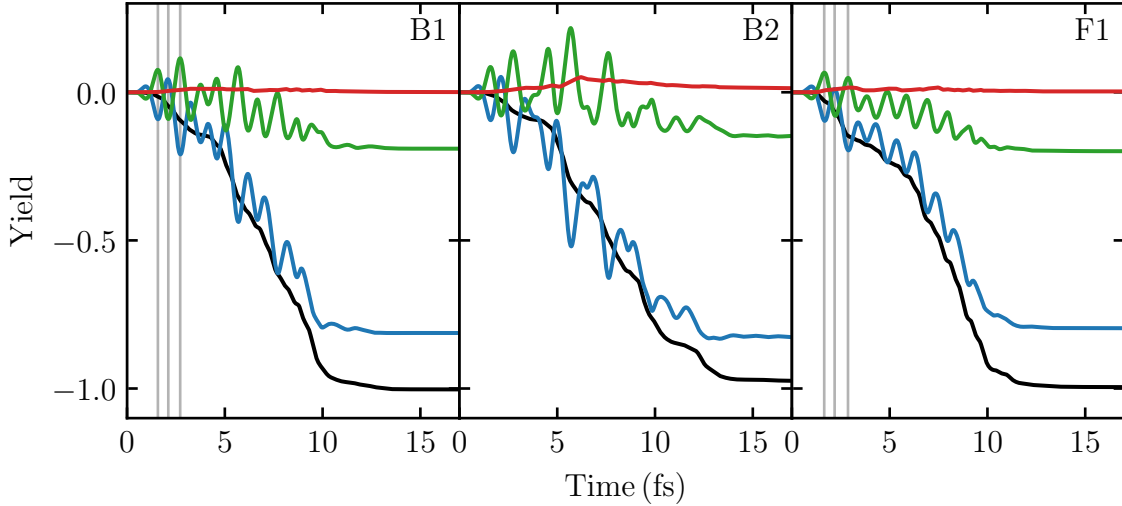


FIG. 8. Time evolution of the electronic yields $Y_V(t)$ (cf. Eq. 15) during the charge migration dynamics from the push-pull dyes towards the TiO_2 semiconductor. The yields are calculated for different Voronoi regions comprising the entire dye (black), its electron releasing (blue) and withdrawing group (green), and the TiO_2 nanocluster (red).

of the photosensitizer enables not only a broad intense sunlight absorption, but also appears to facilitate the electron injection. For the complete picture of the dynamics, a short film of the charge migration process is made available online in the Supplementary Information.

IV. CONCLUSIONS

This contribution is a comparative study analyzing the performance and efficiency of three donor-acceptor π -conjugated dyes as photosensitizers in model solar cells. These chromophores differ by several structural features including two dyes, **B1** and **B2**, with a branched molecular scaffold and one with a pericondensed, fused structure, **F1**. These result in varied degrees of π -conjugation in the dyes, decreasing from **F1** to **B2**. The electronic and spectroscopic characteristics of the dyes attached to a colloidal TiO_2 nanocluster were determined by means of DFT and linear-response TDDFT calculations. From the calculated absorption spectra, it is observed that the absorption maxima of the dyes in the visual region is red-shifted from **B1** to **F1**, which positively influences their sunlight harvesting properties. The MO excitations from the TDDFT spectra unveil that transitions from the HOMO are prevailing for the excited states in the visual region. This confirms the usage of one-electron KS orbitals as the eigenstates of the system with one active electron in the HOMO as an adequate approximation. In addition, the pDOS of the molecular orbitals for the dye, the substrate, and the entire device were computed to confirm their advantageous energetic alignment. In essence, the results reveal that our model systems mimic the fundamental properties of realistic DSSCs and are appropriate to simulate photoinduced charge migration

processes. To supplement the static considerations, the state injection times and currents are evaluated for each DSSC complex. The parameter-free injection times are on the same time scale as the experimental value of 6 fs found for similar systems. The state currents, which includes the state excitation probability, reveals that the **F1** dye yields the highest photocurrents followed by the **B1** chromophore.

Within a time-dependent single active electron approach (TDKS), the laser-induced charge migration process from the dye into the TiO_2 -cluster in the model solar cell is investigated in real time. A broad band excitation of the visual absorption band initiates the electron dynamics from the ground state. The excited electron is injected into the substrate and absorbed by the oxygen atoms at the bottom of the cluster. The population evolution exhibits a variability of the overall injection times, slightly increasing from **F1** to **B2**. This is due to fluctuations between the ground state and a certain subset of excited states. The mechanistic pathway of the electron injection is unveiled with electronic yields which are partitioned for specific molecular fragments. This reveals an oscillation of electron density between the electron donor group to the acceptor group of the dye, with simultaneous injection into the titania cluster. A detailed look at the evolution of the electronic yields shows increased fluctuation of electron density between the electron releasing and withdrawing moieties in **B1** and **B2**. This observation is supported by time-dependent electron density plots at representative time steps. The comparison between one of the branched dyes **B1** and the fused chromophore **F1** confirms the crucial influence of the different structural features on the charge migration process. In particular, it seems that a more weakly electron donor group far away from the interface can play a role in the

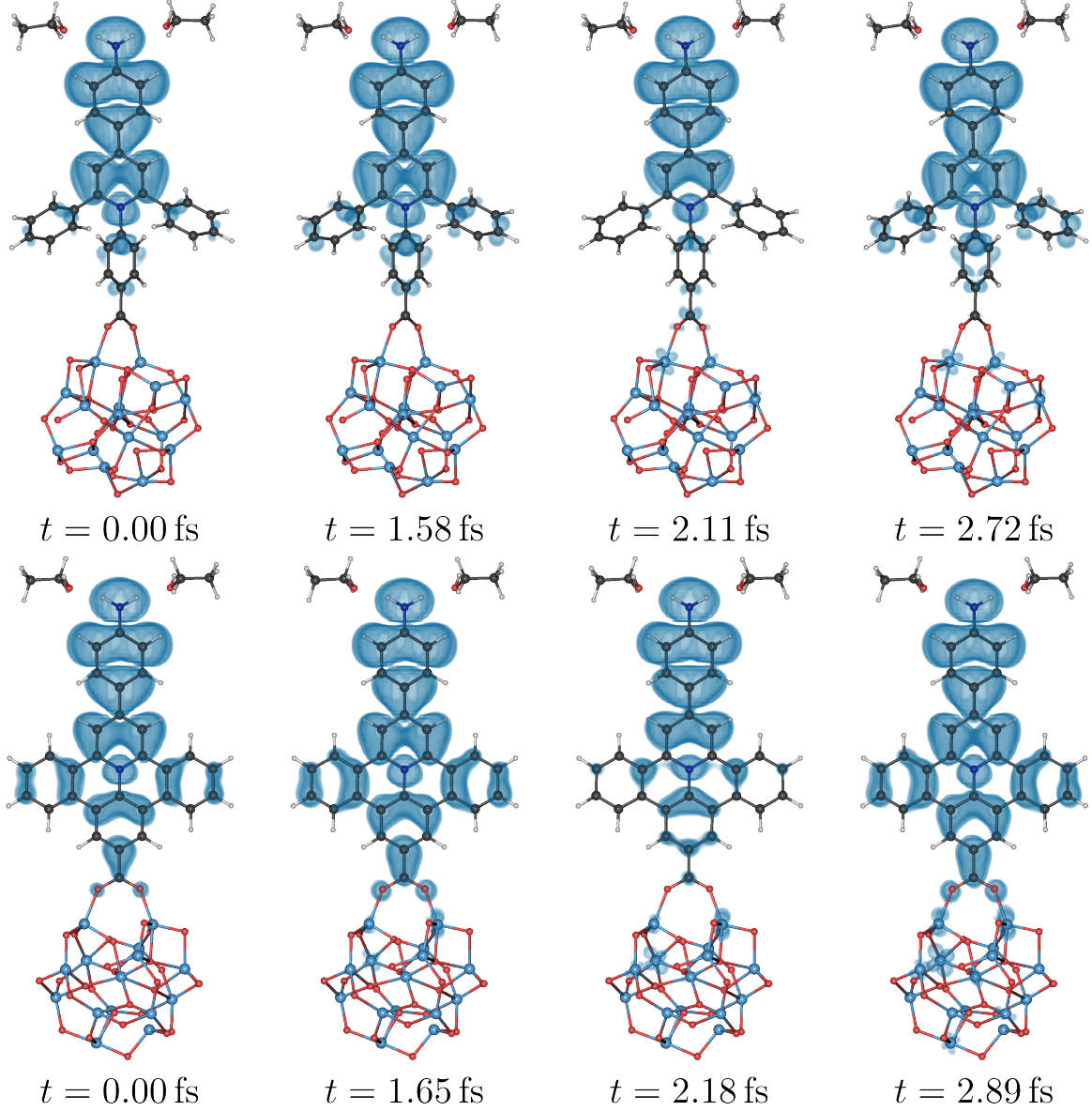


FIG. 9. Evolution of the electron density as blue contour plots for the charge migration from the dye to the titania cluster. A comparison between the structurally branched **B1** and fused chromophore **F1** is shown for four different time steps. These steps are marked in Fig. 8 with gray vertical lines. The contour value is set to 10^{-4} a_0^{-3} . The carbon, hydrogen, nitrogen, oxygen, and titanium atoms are colored dark gray, light gray, blue, red, and cyan, respectively.

injection dynamics. Also, the degree of π -conjugation can be seen to improve the light harvesting properties and the hybridization of the chromophore at the interface, thereby increasing the photovoltaic efficiency of the device.

V. ACKNOWLEDGMENT

The authors thank funding from the Deutsche Forschungsgemeinschaft through project TR1109/2-1

and Hans-Christian Hege for providing the ZIBAmira visualization program. Generous computing resources from the Scientific Computing Services Unit of the Zentraleinrichtung für Datenverarbeitung (ZEDAT) at Freie Universität Berlin are gratefully acknowledged.

- [1] B. O'Regan and M. Grätzel, *Nature* **353**, 737 (1991).
- [2] A. Hagfeldt and M. Grätzel, *Chem. Rev.* **95**, 49 (1995).
- [3] A. Hagfeldt and M. Grätzel, *Acc. Chem. Res.* **33**, 269 (2000).
- [4] M. Grätzel, *Nature* **414**, 338 (2001).
- [5] J. B. Asbury, E. Hao, Y. Wang, H. N. Ghosh, and T. Lian, *J. Phys. Chem. B* **105**, 4545 (2001).
- [6] M. Grätzel, *J. Photochem. Photobiol. C* **4**, 145 (2003).
- [7] A. Hagfeldt, G. Boschloo, L. Sun, L. Kloo, and H. Pettersson, *Chem. Rev.* **110**, 6595 (2010).
- [8] H. Hug, M. Bader, P. Mair, and T. Glatzel, *Appl. Energy* **115**, 216 (2014).
- [9] N.-G. Park, *J. Phys. Chem. Lett.* **4**, 2423 (2013).
- [10] K. Kakiage, Y. Aoyama, T. Yano, K. Oya, J.-i. Fujisawa, and M. Hanaya, *Chem. Commun.* **51**, 15894 (2015).
- [11] Y. Yang, Q. Jin, D. Mao, J. Qi, Y. Wei, R. Yu, A. Li, S. Li, H. Zhao, Y. Ma, L. Wang, W. Hu, and D. Wang, *Adv. Mater.* **29**, 1604795 (2017).
- [12] Z. Yao, M. Zhang, H. Wu, L. Yang, R. Li, and P. Wang, *J. Am. Chem. Soc.* **137**, 3799 (2015).
- [13] J. Schnadt, P. A. Brühwiler, L. Patthey, J. N. O'shea, S. Södergren, M. Odelius, R. Ahuja, O. Karis, M. Bässler, P. Persson, *et al.*, *Nature* **418**, 620 (2002).
- [14] R. Huber, J.-E. Moser, M. Grätzel, and J. Wachtveitl, *J. Phys. Chem. B* **106**, 6494 (2002).
- [15] M. Freitag, F. Giordano, W. Yang, M. Pazoki, Y. Hao, B. Zietz, M. Grätzel, A. Hagfeldt, and G. Boschloo, *J. Phys. Chem. C* **120**, 9595 (2016).
- [16] W. Yang, N. Vlachopoulos, Y. Hao, A. Hagfeldt, and G. Boschloo, *Phys. Chem. Chem. Phys.* **17**, 15868 (2015).
- [17] B. Kılıç, N. Gedik, S. P. Mucur, A. S. Hergul, and E. Gür, *Mater. Sci. Semicond. Process.* **31**, 363 (2015).
- [18] B. Basheer, T. M. Robert, K. Vijayalakshmi, and D. Mathew, *Int. J. Ambient Energy*, 1 (2017).
- [19] S. J. C. Simon, F. G. L. Parlane, W. B. Swords, C. W. Kellett, C. Du, B. Lam, R. K. Dean, K. Hu, G. J. Meyer, and C. P. Berlinguette, *J. Am. Chem. Soc.* **138**, 10406 (2016).
- [20] Y. Chiba, A. Islam, Y. Watanabe, R. Komiya, N. Koide, and L. Han, *Jpn. J. Appl. Phys.* **45**, L638 (2006).
- [21] S. Mathew, A. Yella, P. Gao, R. Humphry-Baker, B. F. Curchod, N. Ashari-Astani, I. Tavernelli, U. Rothlisberger, M. K. Nazeeruddin, and M. Grätzel, *Nature* **6**, 242 (2014).
- [22] D. P. Hagberg, J.-H. Yum, H. Lee, F. De Angelis, T. Marinado, K. M. Karlsson, R. Humphry-Baker, L. Sun, A. Hagfeldt, M. Grätzel, and M. K. Nazeeruddin, *J. Am. Chem. Soc.* **130**, 6259 (2008).
- [23] Y. Ooyama and Y. Harima, *Eur. J. Org. Chem.* **2009**, 2903 (2009).
- [24] A. Mishra, M. K. Fischer, and P. Bäuerle, *Angew. Chem. Int. Ed.* **48**, 2474 (2009).
- [25] M. Pastore, E. Mosconi, F. De Angelis, and M. Grätzel, *J. Phys. Chem. C* **114**, 7205 (2010).
- [26] J. Fortage, C. Peltier, F. Nastasi, F. Puntoriero, F. Tuyéras, S. Griveau, F. Bedioui, C. Adamo, I. Ciofini, S. Campagna, and P. P. Lainé, *J. Am. Chem. Soc.* **132**, 16700 (2010).
- [27] J. Fortage, F. Tuyéras, P. Ochsenein, F. Puntoriero, F. Nastasi, S. Campagna, S. Griveau, F. Bedioui, I. Ciofini, and P. P. Lainé, *Chem. Eur. J.* **16**, 11047 (2010).
- [28] M. Cheng, X. Yang, J. Li, C. Chen, J. Zhao, Y. Wang, and L. Sun, *Chem. Eur. J.* **18**, 16196 (2012).
- [29] T. Le Bahers, F. Labat, T. Pauporté, P. P. Lainé, and I. Ciofini, *J. Am. Chem. Soc.* **133**, 8005 (2011).
- [30] T. Le Bahers, T. Pauporté, P. P. Lainé, F. Labat, C. Adamo, and I. Ciofini, *J. Phys. Chem. Lett.* **4**, 1044 (2013).
- [31] U. Mehmood, I. A. Hussein, M. Daud, S. Ahmed, and K. Harrabi, *Dyes Pigm.* **118**, 152 (2015).
- [32] K. Chaitanya, X.-H. Ju, and B. M. Heron, *RSC Adv.* **4**, 26621 (2014).
- [33] F. Ambrosio, N. Martsinovich, and A. Troisi, *J. Phys. Chem. C* **116**, 2622 (2012).
- [34] S.-H. Liu, H. Fu, Y.-M. Cheng, K.-L. Wu, S.-T. Ho, Y. Chi, and P.-T. Chou, *J. Phys. Chem. C* **116**, 16338 (2012).
- [35] J. Yang, X. Wang, W.-L. Yim, and Q. Wang, *J. Phys. Chem. C* **119**, 26355 (2015).
- [36] T. Gomez, F. Jaramillo, E. Schott, R. Arratia-Pérez, and X. Zarate, *Solar Energy* **142**, 215 (2017).
- [37] M. Planells, L. Pellejà, J. N. Clifford, M. Pastore, F. De Angelis, N. López, S. R. Marder, and E. Palomares, *Energy Environ. Sci.* **4**, 1820 (2011).
- [38] J. C. Brauer, A. Marchioro, A. A. Paraecattil, A. A. Os-kouei, and J.-E. Moser, *J. Phys. Chem. C* **119**, 26266 (2015).
- [39] K. R. Siefermann, C. D. Pemmaraju, S. Neppel, A. Shavorskiy, A. A. Cordones, J. Vura-Weis, D. S. Slaughter, F. P. Sturm, F. Weise, H. Bluhm, M. L. Strader, H. Cho, M.-F. Lin, C. Bacellar, C. Khurmi, J. Guo, G. Coslovich, J. S. Robinson, R. A. Kaindl, R. W. Schoenlein, A. Belkacem, D. M. Neumark, S. R. Leone, D. Nordlund, H. Ogawara, O. Krupin, J. J. Turner, W. F. Schlotter, M. R. Holmes, M. Messerschmidt, M. P. Minitti, S. Gul, J. Z. Zhang, N. Huse, D. Prendergast, and O. Gessner, *J. Phys. Chem. Lett.* **5**, 2753 (2014).
- [40] L. Zhang, L. Favereau, Y. Farre, A. Maufroy, Y. Pellegrin, E. Blart, M. Hissler, D. Jacquemin, F. Odobel, and L. Hammarström, *RSC Adv.* **6**, 77184 (2016).
- [41] W. R. Duncan and O. V. Prezhdo, *Annu. Rev. Phys. Chem.* **58**, 143 (2007).
- [42] N. Martsinovich and A. Troisi, *Energy Environ. Sci.* **4**, 4473 (2011).
- [43] T. Le Bahers, T. Pauporté, G. Scalmani, C. Adamo, and I. Ciofini, *Phys. Chem. Chem. Phys.* **11**, 11276 (2009).
- [44] X. Zarate, S. Schott-Verdugo, A. Rodriguez-Serrano, and E. Schott, *J. Phys. Chem. A* **120**, 1613 (2016).
- [45] T. Gomez, G. Hermann, X. Zarate, J. F. Pérez-Torres, and J. C. Tremblay, *Molecules* **20**, 13830 (2015).
- [46] G. Hermann and J. C. Tremblay, *J. Phys. Chem. C* **119**, 25606 (2015).
- [47] G. Hermann and J. Tremblay, *J. Chem. Phys.* **145**, 174704 (2016).
- [48] V. Pohl, G. Hermann, and J. C. Tremblay, *J. Comput. Chem.* (2017), 10.1002/jcc.24792.
- [49] H. Park, E. Bae, J.-J. Lee, J. Park, and W. Choi, *J. Phys. Chem. B* **110**, 8740 (2006).
- [50] J. Rochford, D. Chu, A. Hagfeldt, and E. Galoppini, *J. Am. Chem. Soc.* **129**, 4655 (2007).

- [51] R. Sánchez-de Armas, J. Oviedo López, M. A. San-Miguel, J. F. Sanz, P. Ordejón, and M. Pruneda, *J. Chem. Theory Comput.* **6**, 2856 (2010).
- [52] E. Schrödinger, *Ann. der Physik* **386**, 109 (1926).
- [53] J. B. Foresman, M. Head-Gordon, J. A. Pople, and M. J. Frisch, *J. Phys. Chem.* **96**, 135 (1992).
- [54] J. C. Tremblay and T. Carrington Jr., *J. Chem. Phys.* **121**, 11535 (2004).
- [55] J. C. Tremblay, T. Klamroth, and P. Saalfrank, *J. Chem. Phys.* **129**, 084302 (2008).
- [56] J. C. Tremblay, S. Klinkusch, T. Klamroth, and P. Saalfrank, *J. Chem. Phys.* **134**, 044311 (2011).
- [57] J. Li, I. Kondov, H. Wang, and M. Thoss, *J. Phys. Chem. C* **114**, 18481 (2010).
- [58] C. Fonseca Guerra, J.-W. Handgraaf, E. J. Baerends, and F. M. Bickelhaupt, *J. Comput. Chem.* **25**, 189 (2004).
- [59] I. Barth, H.-C. Hege, H. Ikeda, A. Kenfack, M. Koppitz, J. Manz, F. Marquardt, and G. K. Paramonov, *Chem. Phys. Lett.* **481**, 118 (2009).
- [60] C. Adamo and V. Barone, *J. Chem Phys.* **110**, 6158 (1999).
- [61] A. Schäfer, H. Horn, and R. Ahlrichs, *J. Chem. Phys.* **97**, 2571 (1992).
- [62] F. Weigend and R. Ahlrichs, *Phys. Chem. Chem. Phys.* **7**, 3297 (2005).
- [63] S. Grimme, J. Antony, S. Ehrlich, and H. Krieg, *J. Chem. Phys.* **132**, 154104 (2010).
- [64] S. Grimme, S. Ehrlich, and L. Goerigk, *J. Comput. Chem.* **32**, 1456 (2011).
- [65] A. Klamt, *J. Phys. Chem.* **99**, 2224 (1995).
- [66] F. Eckert and A. Klamt, *AIChE J.* **48**, 369 (2002).
- [67] A. Klamt, V. Jonas, T. Bürger, and J. C. Lohrenz, *J. Phys. Chem. A* **102**, 5074 (1998).
- [68] “Cosmotherm, Version C3.0, Release 13.01, COSMOlogic GmbH & Co. KG,” (2013), <http://www.cosmologic.de>.
- [69] E. Gross and W. Kohn, *Adv. Quantum Chem.* **21**, 287 (1990).
- [70] H. Li, Y. Li, and M. Chen, *RSC Adv.* **4**, 57916 (2014).
- [71] C.-L. Wang, J. Wang, F.-Q. Bai, J. Chen, and H.-X. Zhang, *Int. J. Quantum Chem.* **114**, 560 (2014).
- [72] “TURBOMOLE V6.5, a development of University of Karlsruhe and Forschungszentrum Karlsruhe GmbH, 1989-2007, TURBOMOLE GmbH, since 2007,” (2013), available via <http://www.turbomole.com>.
- [73] G. Hermann, V. Pohl, J. C. Tremblay, B. Paulus, H.-C. Hege, and A. Schild, *J. Comput. Chem.* **37**, 1511 (2016).
- [74] D. Stalling, M. Westerhoff, and H.-C. Hege, in *Visualization Handbook*, edited by C. D. Hansen and C. R. Johnson (Elsevier, Amsterdam, 2005) Chap. 8, pp. 749–767.
- [75] J. D. Hunter, *Comput. Sci. Eng.* **9**, 90 (2007).
- [76] L. Dworak, V. V. Matyilitsky, and J. Wachtveitl, *ChemPhysChem* **10**, 384 (2009).
- [77] Y. Ooyama, M. Kanda, K. Uenaka, and J. Ohshita, *ChemPhysChem* **16**, 3049 (2015).